

Dark Endmember in Spectral Feature Space under Variable Atmosphere

K.-Y. Choi

*Environment Agency
Science Group – Technology,
Lower Bristol Road
Bath BA2 9ES
UK
reno.choi@environment-agency.gov.uk*

Edward J. Milton

*School of Geography
University of Southampton
Highfield
Southampton SO17 1BJ
UK
E.J.Milton@soton.ac.uk*

Abstract

One of the most important assumptions in most multispectral image transformation methods is that the position of the dark endmember is placed at the origin of the n -D spectral feature space regardless of the target spectral signature. A series of field experiments under varying illumination resulted that ‘shadow-lines’, which hypothetically pass through the dark endmember, never pass directly through the origin of the spectral feature space. A conceptual radiative transfer model was derived and demonstrated its susceptibility to the proportion of scattered light from the sky. The model showed that the location of the dark endmember, defined as the ‘*dark point virtual endmember* (DPVE)’, is assumed to be sensitive to the state of atmosphere. Further analysis also revealed that the DPVE plays an important role in defining the data distribution in spectral feature space. This study suggested that accurate estimation of DPVE could enable to reduce some of the uncertainties associated with conventional dark point atmospheric correction methods.

1 Introduction

The atmospheric effect on the spectral radiance of the Earth’s surface is a frequent problem for quantitative studies using remote sensing. Most image correction methods either over- or underestimate predictions due to broad definitions of atmospheric condition or require ancillary *in situ* information for model input parameters. With respect to the operational aspects of remote sensing, atmospheric correction methods using the concept of ‘*Dark Object Subtraction* (DOS)’ have been studied over many years (Chavez, 1988; Kaufman and Sendra, 1988; Kaufman et al., 1997; Moran et al., 2001; Smith and Milton, 1999), on the basis of the fact that, if reflectance of a ground target is small enough, the signal contributed from atmospheric effect is maximised. However, the accuracy and reliability of the dark target method is dependent upon the accurate estimation of spectral signature of dark object. These properties are conceptualised as the ‘*dark point endmember*’.

The concept of the dark point endmember also plays an important role in quantitative studies of multi- or hyper-spectral remote sensing. It is widely used technique, not only because it allows distinguishing unique spectral signatures from the Earth’s surface within an image, but also it is an effective in reducing undesirable effects, such as those resulting from non-uniform illumination due to variations in topography with relatively simple way. One of the most important assumptions in such band ratio based image processing is that the position of the dark

endmember is placed at the origin of the n -D spectral feature space regardless of the target spectral signature. In an ideal world this assumption is true, but whether for the nature of the phenomena being investigated or because of the state of atmosphere, the dark endmember may lie outside the cloud of points forming the image data.

The objective of this paper is to investigate the hypothesis that the apparent reflectance of the dark point endmember is determined by the temporal variability of the atmosphere. The dark point endmember is a hypothetical position in the multispectral dimension (Choi and Milton, 1999), from which entire data points of image pixels radiate away (Craig, 1994). As the theoretical dark point represents sensor response to a zero spectral reflectance of any ground targets, it is darker than any other pixels in image and is closer in concept to a virtual endmember as described by (Tompkins et al., 1997) or to the ‘point of all shadow’ (Kauth and Thomas, 1976). The dark endmember is defined as the ‘*dark point virtual endmember* (DPVE)’ and its location is assumed to be sensitive to the state of atmosphere.

To identify the DPVE position, iso-lines resulting from variable illumination over the same ground targets is defined as ‘*shadow-line*’, and the following two assumptions are made, 1) shadow-line is linear in n -D spectral feature space, and 2) it passes through a DPVE as it becomes darker until no direct illumination. A conceptual model based on radiative transfer theory simulates shadow-lines observed from intensive field spectroradiometer measurements. The assumption of the DPVE at the origin of spectral feature space enables conventional multispectral image transformation methods to be effective in reducing uncertainties induced by variable atmosphere

2 Field Spectral Experiments

2.1 Acquisition of spectral radiances under variable atmosphere

Field experiments were designed to investigate spectral changes of reflected radiance under variable illumination. The contribution of atmosphere for remotely sensed signal in homogeneous Lambertian surface is expressed by several atmospheric parameters (Vermote et al., 1997),

$$\rho_* = T_g \left(\rho_a + \frac{\rho_t}{1 - \rho_t S} T_s T_v \right) \quad (1)$$

ρ_* : Apparent reflectance at top of atmosphere (TOA)

ρ_a : Intrinsic atmospheric reflectance

ρ_t : Inherent reflectance at ground

T_g : Gaseous transmittance

S : Atmospheric spherical albedo

T_x : Normalised transmittance at sensing geometry ($x=s$ or v)

where atmospheric spherical albedo, S , is a function of Rayleigh and aerosol scattering and the Sun angle, μ , where $\cos(\theta_s)$. The normalized transmittance, T_x , consists of direct ($e^{-\tau/\mu_x}$) and diffused ($t_d(\theta_x)$) components of normalized incident solar irradiance.

Since the illumination from the Sun is determined by transmittance of incident solar irradiance, T_s (i.e. decreasing direct incident solar irradiance, $e^{-\tau/\mu_x}$, under shadow), other variables in Equation (1) are intended not to change during the experiment. Data acquisition under fast moving patches of cloud shadow in a fixed position enabled us to assume constant Sun

angle (μ_s), target reflectance (ρ_t), and gaseous transmittance (T_g).

A hyperspectral and a broadband multispectral field radiometers were used for continuous recordings while series of patches of cloud were passing over the sites: ASD FieldSpec Pro (wavelength range of 350~2500nm with 10nm resolution) and a Milton Multiband Radiometer (Milton, 1980). Both instruments were calibrated with NPL traceable standards. The instruments were setup in the Common and the University campus in Southampton, UK. Reflected radiance from four ground targets were acquired in July 2001 (Table 1).

Sets of shadow boundary regions with large enough illumination changes at sufficient period were selected among the original time series data. No spectra, except water absorption regions at 1400 and 1900nm, were found to have zero values, i.e. no true darkness, even under the darkest shadows during the measurements.

Table 1. A list of ground targets used during the field measurements. The measurements were taken in the various places, Southampton, UK.

Target	Description	No. of shadow boundaries	Location
Grass	Fresh and dense recently mown grass	6	
Dried grass	Dense patch surrounded by healthy grass	7	The Common
Asphalt	Worn-out asphalt target in the parking	7	
Pebbles	Pebbles in a pedestrian street	5	Univ. of Southampton

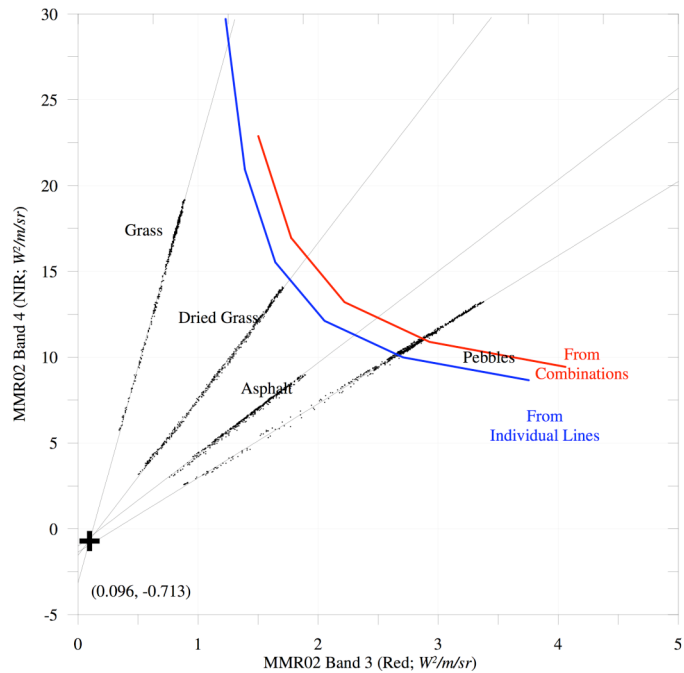


Figure 1. Shadow-lines of data acquired with a 4-channel radiometer (MMR) during the field experiments. The point with a symbol \oplus represents the DPVE derived by median of \Re 's from individual shadow-lines.

2.2 Spectral variation in shadow boundaries

Selected shadow boundaries projected in 2-D feature space show that the spectral response under decreasing illumination condition tends to converge at the origin with very strong linear relationship from both instruments, defined as *shadow-line* (**Figure 1**). Scatter plots for all targets in 640nm (x-axis) and 800nm (y-axis) have linear regressions on the data with r^2 value of greater than 0.9 and the ranges of 95% confident limits are narrow. However, it is important to notice that no intercepts of shadow-lines pass through the origin.

The linear regression analysis was extended over the whole spectral range of ASD, except two strong water absorption regions, i.e. 1300~1500 and 1800~2000nm. Wavelength of 1600nm was used as the dependent variable Y , while the spectral signal in wavelengths shorter than 1600nm was treated as the independent variable X . The reason for choosing 1600nm that was relatively unaffected by atmospheric effects, yet its radiometric value was large enough to provide a reasonable signal-to-noise ratio.

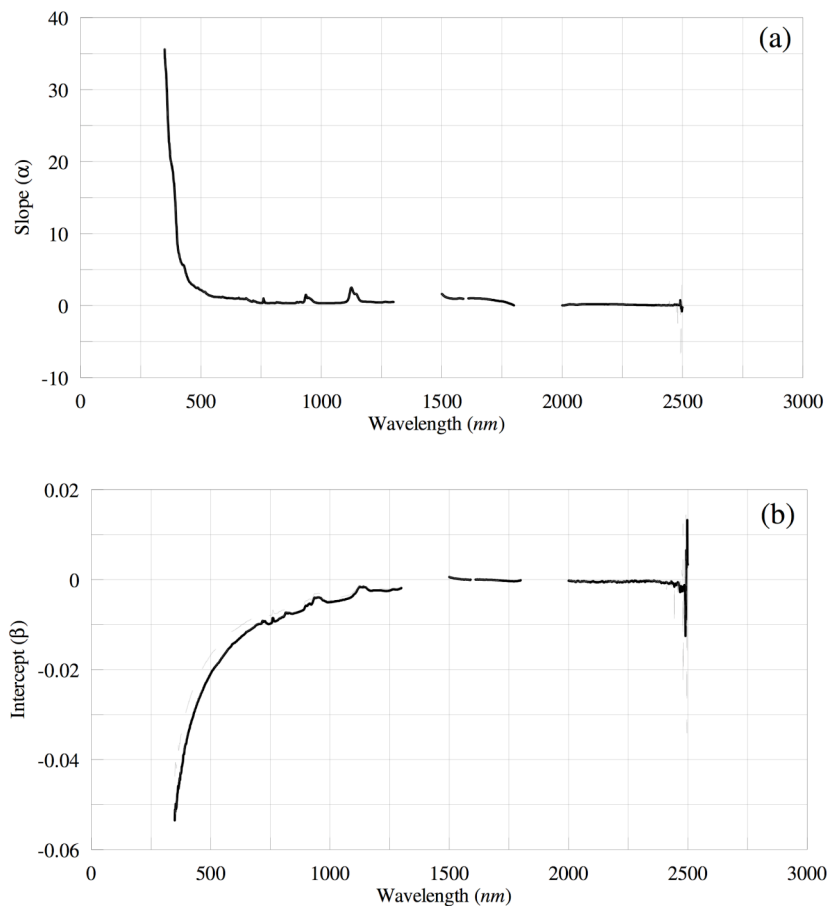


Figure 2. Typical slope (a) and intercept (b) spectra of regression lines with reference wavelength at 1600nm from grass target. Solid plots represent median, while upper and lower grey ones are for 25 and 75% of quartile, respectively.

There were distinctive spectral dependencies in shadow-lines regarding their position (**Figure 2**). The slopes of shadow-line in the short wavelength region follow target dependent sharp exponential curve (larger gradient for vegetation target). Slight increases of slope value were found in two water absorption regions at around 900 and 1150nm. The intercept in this paper defines the value in dependent variable Y , as the independent variable X equals zero. Spectra of intercept of shadow-line are target dependent and shows negative exponential curve

with much more steady trend than slope, until it reaches near zero at longer wavelength. The ranges between 25 and 75% quartiles for shadow-line intercept vary depending upon target types and are relatively wider at lower wavelength, while those in shadow-line slope are narrower over whole spectral region.

Despite very strong relationship by r^2 , the coefficient of determination (greater than 0.98 for all targets), further analysis was conducted to check whether the dataset contains nonlinearity, as previous studies have shown that nonlinear mixing, such as between vegetation and background soil, is observed in spectral feature space (Law and Waring, 1994; Ray and Murray, 1996). The normalized F value, which tests the null hypothesis by the analysis of variance (ANOVA) from both linear and higher order polynomial regression (Kleinbaum et al., 1998), illustrated that statistically there is no nonlinearity for all targets at any wavelength, indicating that the field data are considered as pure spectral signature.

The similarity between shadow-lines of each target was examined by F test adopted from an analysis of covariance (*ANCOVA*) (Sokal and Rohlf, 1995). The hypothesis tested was that the slope of shadow-line was unaffected by atmospheric condition in each shadow boundary. As normalized F value for all targets were greater than 1.0, the hypothesis was rejected and the shadow-lines among groups of shadow boundary are statistically different. Even within short time scale, less than an order of minutes, shadow-lines are sensitive to the temporal variability of atmosphere.

3 Shadow-line in Spectral Feature Space

3.1 Single shadow-line

For a shadow-line in 2-D feature space, at least two reflected spectra of a target under different illumination are required. The model adopted a method developed by (Piech and Walker, 1974), obtaining atmospheric parameters by using pixels with different local illumination condition in scene shadows, under the conditions with identical ground target in each shadow boundary and ignoring variability of adjacency effect. Bright (\circ) and dark (\bullet) symbols are added to a pair of apparent reflectance (Equation (1)) under different illumination condition. Since inherent target reflectance, ρ_t , is identical in both cases, it is eliminated from the equations. The relationship between spectral responses at shadow boundary region, ρ_*° and ρ_*^\bullet , is derived as,

$$\rho_*^\bullet = \sigma \rho_*^\circ + \rho_a T_g (1 - \sigma) + (S^\bullet - S^\circ) \frac{\xi}{T_v T_g T_s} \quad (2)$$

where $\xi = \rho_a^2 T_g^2 - (\rho_*^\circ + \rho_*^\bullet) \rho_a T_g + \rho_*^\circ \rho_*^\bullet$ and $\sigma = T_s^\bullet / T_s^\circ$ (Diffuse-to-global transmittance ratio, D:G). If nonlinear term, ξ , is ignored in this study due to an assumption made earlier, i.e. $S^\bullet - S^\circ \approx 0$, apparent reflectance ρ_*° and ρ_*^\bullet represent a linear relationship (Piech and Walker, 1974).

There is a pair of Equation (2) for two spectral bands, m and n ,

$$\rho_{*\lambda_m}^\bullet = \frac{T_{s\lambda_m}^\bullet}{T_{s\lambda_m}^\circ} \rho_{*\lambda_m}^\circ + \rho_{a\lambda_m} T_{g\lambda_m} \left(1 - \frac{T_{s\lambda_m}^\bullet}{T_{s\lambda_m}^\circ} \right), \quad \rho_{*\lambda_n}^\bullet = \frac{T_{s\lambda_n}^\bullet}{T_{s\lambda_n}^\circ} \rho_{*\lambda_n}^\circ + \rho_{a\lambda_n} T_{g\lambda_n} \left(1 - \frac{T_{s\lambda_n}^\bullet}{T_{s\lambda_n}^\circ} \right) \quad (3)$$

Equation (3) are used to locate data points under two illuminations in 2-D spectral space (wavebands denoted as λ_m and λ_n , where $m < n$), and expressed as,

$$\rho_{*\lambda_n} = a\rho_{*\lambda_m} + b \quad (4)$$

where, a is slope and intercept, b . While the intercept is the offset value of $\rho_{*\lambda_n}$ as $\rho_{*\lambda_n} = 0$, the slope is the ratio of distances between bright and dark in two spectral bands. The slope and intercept are rewritten,

$$a = \left(\frac{\rho_{*\lambda_n}^* - \rho_{a\lambda_n} T_{g\lambda_n}}{\rho_{*\lambda_m}^* - \rho_{a\lambda_m} T_{g\lambda_m}} \right) \cdot \mathfrak{R}, \quad (5)$$

$$b = \rho_{*\lambda_n}^* (1 - \mathfrak{R})$$

where, $\mathfrak{R} = (1 - \sigma_{\lambda_n}) / (1 - \sigma_{\lambda_m})$, a function of ratios of atmospheric transmittances for both spectral bands. Since $\rho_{*\lambda_n}^* \neq 0$ and $\sigma \neq 1$, there are two conditions for zero intercept (for ideal condition): either $\sigma_{\lambda_m} = \sigma_{\lambda_n}$ or $t_{d\lambda_m}(\theta_s) = t_{d\lambda_n}(\theta_s) = 0$ (Equation (1)). Both of which are unrealistic unless there is no atmospheric interaction, such as laboratory condition, or taking into account accurately estimated diffused irradiance in the atmosphere.

Contribution of such atmospheric effects on both slope and intercept of shadow-line are investigated with the results from earlier analytical test with field measurements. Since the slope of shadow-line is always positive ($a > 0$), and that the intercept b in VNIR is below zero, the term \mathfrak{R} should always be $\mathfrak{R} > 1$. If \mathfrak{R} is increasing, the slope of the shadow-line increases while the intercept decreases. This inverse relationship between slope and intercept is also true, when rewrite Equation (4) as $b = -\rho_{*\lambda_m} \cdot a + \rho_{*\lambda_n}$. The result shows the statistically different shadow-lines in a group of shadow boundaries on each target shown earlier, and \mathfrak{R} as a function of diffused irradiance is directly related to changes of shadow-line.

3.2 Two shadow-lines and dark point

With at least two shadow-lines from different ground targets, the point of interception of the shadow-lines will be defined as DPVE that is darker than any data possibly measured. **Figure 3** shows the shadow-lines passing close to the origin. In this particular dataset, shadow-lines do not meet in a single point though very close, since each shadow-lines data was obtained in different time and date, i.e. under different atmospheric condition.

In 2-D feature space, a DPVE from two shadow-lines are found by substituting the interception point $(\rho_{\lambda_m}^{dpve}, \rho_{\lambda_n}^{dpve})$ into Equation (4), and rewrite without intrinsic atmospheric reflectance ($\rho_a = 0$), i.e. for ground measurement,

$$\rho_{\lambda_m}^{dpve} = \frac{\rho_{*\lambda_{m1}}^* \rho_{*\lambda_{m2}}^* \cdot (\rho_{*\lambda_{m1}}^* - \rho_{*\lambda_{m2}}^*)}{\rho_{*\lambda_{m1}}^* \rho_{*\lambda_{n2}}^* - \rho_{*\lambda_{n1}}^* \rho_{*\lambda_{m2}}^*} \left(\frac{1}{\mathfrak{R}} - 1 \right) \quad (6)$$

$$\rho_{\lambda_n}^{dpve} = \frac{\rho_{*\lambda_{n1}}^* \rho_{*\lambda_{n2}}^* \cdot (\rho_{*\lambda_{m1}}^* - \rho_{*\lambda_{m2}}^*)}{\rho_{*\lambda_{m1}}^* \rho_{*\lambda_{n2}}^* - \rho_{*\lambda_{n1}}^* \rho_{*\lambda_{m2}}^*} (1 - \mathfrak{R})$$

If two shadow-lines are not identical ($\rho_{*\lambda_{m1}}^* \neq \rho_{*\lambda_{m2}}^*$ and $\rho_{*\lambda_{n1}}^* \neq \rho_{*\lambda_{n2}}^*$), \mathfrak{R} should equal 1.0 for the DPVE at the origin. The value \mathfrak{R} was computed from the *in situ* data by (**Figure 3**) any pair of available ground targets with the DPVE model (Equation (6)) and using known slopes and intercepts of each shadow-line (Equation (5)).

Although \mathfrak{R} values from the method with a pair of ground targets resulted more variable, the median of each method were very close (the \mathfrak{R} from the DPVE model (red) is close to the one from the individual shadow-line model (blue)). The relatively wide distributions in the first case was mainly because the atmospheric conditions for the measurements of each target were not identical.

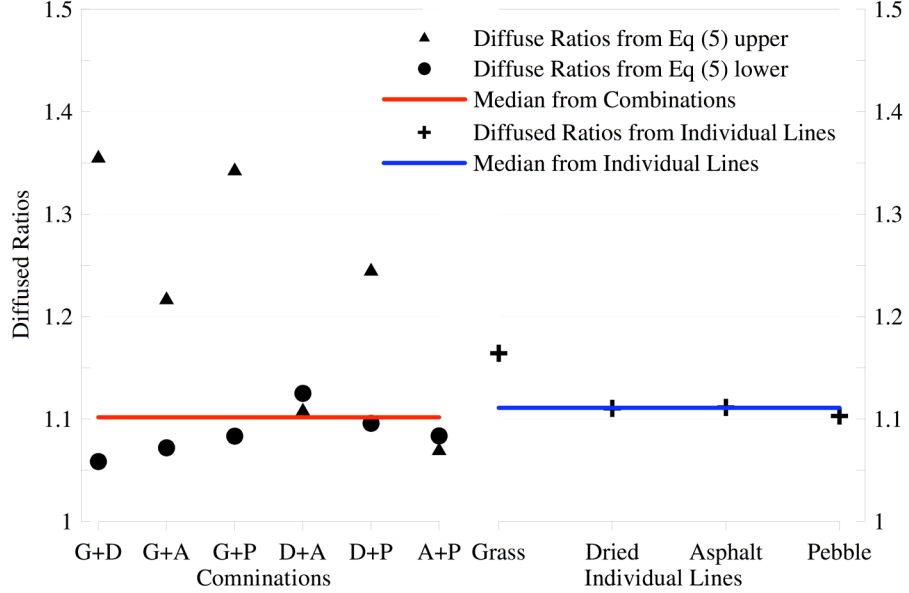


Figure 3. Comparisons of \mathfrak{R} from the DPVE models and the shadow-line model by using the SSB measured on the ground. Since the DPVE model requires two shadow-lines, all possible combinations from available targets (G: Grass, D: Dried grass, A: Asphalt, and P: Pebbles) were applied in the left side of the plot. Each symbol in the plot represent \mathfrak{R} from $\rho_{\lambda_m}^{dpve}$ (\blacktriangle), $\rho_{\lambda_n}^{dpve}$ (\bullet), and each individual shadow-line ($+$).

4 Conclusion

Analysis of field data and a conceptual model showed that defining non-origin shadow-lines and a DPVE are controlled by the atmospheric condition, \mathfrak{R} , a ratio of D:G of two spectral bands. As a reverse approach, the atmospheric effect on a scene with spatially uniform \mathfrak{R} is to be obtained by identifying DPVE regardless of target spectra. Moreover, \mathfrak{R} plays an important role of determining boundary of entire scatter diagram in spectral feature space. From Eq. (4), the maximum radiances for shadow-lines for field data are,

$$\begin{aligned}\rho_{\lambda_m}^{\circ Max} &= \frac{b\mathfrak{R}}{a(1-\mathfrak{R})} \\ \rho_{\lambda_n}^{\circ Max} &= a\rho_{\lambda_m}^{\circ Max} + b\end{aligned}\quad (6)$$

With two \mathfrak{R} s from above, continuous maximum radiance lines superimposed (**Figure 1**) illustrated that variability of DPVE position due to atmospheric effects determines the cone-shape scatter diagram typically shown in remotely sensed data. Under no atmospheric condition ($\mathfrak{R} = 1$), $(\rho_{\lambda_m}^{\circ Max}, \rho_{\lambda_n}^{\circ Max})$ becomes infinite, whereas the cone tends to shrink to DPVE with more atmospheric constraint ($\mathfrak{R} > 1$).

5 Acknowledgement

The authors are gratefully acknowledged the loan of the ASD FieldSpec Pro and the MMR from NERC Equipment Pool for Field Spectroscopy (NERC EPFS) from University of Southampton, UK, and Bill Damon for technical support throughout this project. This work had been funded through a bursary to Kyu-Young Choi from the University of Southampton High Performance Computing Initiative.

6 References

Chavez, P.S., 1988. An improved dark-object subtraction technique for atmospheric scattering correction of multispectral data. *Remote Sensing of Environment*, 24(3): 459-479.

Choi, K.-Y. and Milton, E.J., 1999. A multispectral transform for the suppression of cloud shadows, The Fourth International Airborne Remote Sensing Conference and exhibition / 21st Canadian Symposium on Remote Sensing. ERIM International Inc., Ottawa, Canada, pp. 762-769.

Craig, M.D., 1994. Minimum-Volume Transforms for Remotely-Sensed Data. *IEEE Transactions on Geoscience and Remote Sensing*, 32(3): 542-552.

Kaufman, Y.J. and Sendra, C., 1988. Algorithm for Automatic Atmospheric Corrections to Visible and Near-Ir Satellite Imagery. *International Journal of Remote Sensing*, 9(8): 1357-1381.

Kaufman, Y.J. et al., 1997. The MODIS 2.1-mu m channel - Correlation with visible reflectance for use in remote sensing of aerosol. *Ieee Transactions on Geoscience and Remote Sensing*, 35(5): 1286-1298.

Kauth, R.J. and Thomas, G.S., 1976. The tasseled cap - a graphic description of the spectral-temporal development of agricultural crops as seen by Landsat, The 3rd Symposium on Machine Processing of Remotely Sensed Data. LARS, Purdue University, Lafayette, IN, pp. 41-49.

Kleinbaum, D.G., Kupper, L.L., Muller, K.E. and Nizam, A., 1998. Applied regression analysis and other multivariable methods. Duxbury Press, California, 798 pp.

Law, B.E. and Waring, R.H., 1994. Remote-Sensing of Leaf-Area Index and Radiation Intercepted by Understory Vegetation. *Ecological Applications*, 4(2): 272-279.

Milton, E.J., 1980. A Portable Multiband Radiometer for Ground Data Collection in Remote Sensing. *International Journal of Remote Sensing*, 1(2): 153-165.

Moran, M.S. et al., 2001. A refined empirical line approach for reflectance factor retrieval from Landsat-5 TM and Landsat-7 ETM+. *Remote Sensing of Environment*, 78(1-2): 71-82.

Piech, K.R. and Walker, J.E., 1974. Interpretation of Soils. *Photogrammetric Engineering and Remote Sensing*, 40: 87-94.

Ray, T.W. and Murray, B.C., 1996. Nonlinear spectral mixing in desert vegetation. *Remote Sensing of Environment*, 55(1): 59-64.

Smith, G.M. and Milton, E.J., 1999. The use of the empirical line method to calibrate remotely sensed data to reflectance. *International Journal of Remote Sensing*, 20(13): 2653-2662.

Sokal, R.R. and Rohlf, F.J., 1995. *Biometry: The principles and practice of statistics in biological research*. W.H. Freeman and Company, New York, 887 pp.

Tompkins, S., Mustard, J.F., Pieters, C.M. and Forsyth, D.W., 1997. Optimization of endmembers for spectral mixture analysis. *Remote Sensing of Environment*, 59(3): 472-489.

Vermote, E.F., Tanre, D., Deuze, J.L., Herman, M. and Morcrette, J.J., 1997. Second Simulation of the Satellite Signal in the Solar Spectrum, 6S: An overview. *IEEE Transactions on Geoscience and Remote Sensing*, 35(3): 675-686.